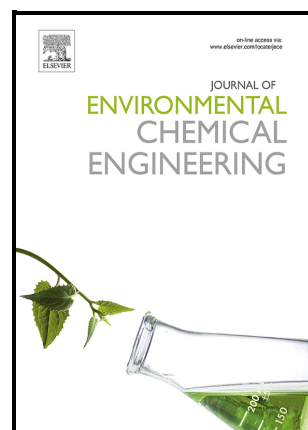# Journal Pre-proof

Highly active iron phosphide catalysts for selective electrochemical nitrate reduction to ammonia

Takwa Chouki, Manel Machreki, Iwona A. Rutkowska, Beata Rytelewska, Pawel J. Kulesza, Georgi Tyuliev, Moussab Harb, Luis Miguel Azofra, Saim Emin

Please cite this article as: Takwa Chouki, Manel Machreki, Iwona A. Rutkowska, Beata Rytelewska, Pawel J. Kulesza, Georgi Tyuliev, Moussab Harb, Luis Miguel Azofra and Saim Emin, Highly active iron phosphide catalysts for selective electrochemical nitrate reduction to ammonia, *Journal of Environmental Chemical Engineering,* (2022) doi:https://doi.org/10.1016/j.jece.2023.109275

This is a PDF file of an article that has undergone enhancements after acceptance, such as the addition of a cover page and metadata, and formatting for readability, but it is not yet the definitive version of record. This version will undergo additional copyediting, typesetting and review before it is published in its final form, but we are providing this version to give early visibility of the article. Please note that, during the production process, errors may be discovered which could affect the content, and all legal disclaimers that apply to the journal pertain.

Highly active iron phosphide catalysts for selective electrochemical nitrate reduction to ammonia

Takwa Chouki [a], Manel Machreki [a], Iwona A. Rutkowska [b], Beata Rytelewska [b], Pawel J. Kulesza [b], Georgi Tyuliev [c], Moussab Harb [d, e], Luis Miguel Azofra [f], Saim Emin [a, *]

a. Materials Research Laboratory, University of Nova Gorica, Ajdovscina 5270, Slovenia.

b. Faculty of Chemistry, University of Warsaw, Pasteura 1, 02-093 Warsaw, Poland.

c. Institute of Catalysis, Bulgarian Academy of Science, Sofia 1113, Bulgaria.

d. KAUST Catalysis Center (KCC), Physical Sciences and Engineering Division (PSE), King Abdullah University of Science and Technology (KAUST), Thuwal 23955-6900, Saudi Arabia.

e. QSARLab Ltd., Trzy Lipy 3, 80-172 Gdańsk, Poland

f. Instituto de Estudios Ambientales y Recursos Naturales (i-UNAT), Campus Universitario de Tafira, Universidad de Las Palmas de Gran Canaria (ULPGC), Las Palmas de Gran Canaria, Spain.

*Corresponding author. *E-mail address*: saim.emin@ung.si (S. Emin)

ABSTRACT

The electrochemical reduction reaction of the nitrate ion (NO_3^-), a widespread water pollutant, to valuable ammonia (NH_3) is a promising approach for environmental remediation and green energy conservation. The development of high-performance electrocatalysts to selectively reduce NO_3^- wastes into value-added NH_3 will open up a different route of NO_3^- treatment, and impose both environmental and economic impacts on sustainable NH_3 synthesis. Transition metal phosphides represent one of the most promising earth-abundant catalysts with impressive electrocatalytic activities. Herein, we report for the first time the electrocatalytic reduction of NO_3^- using different phases of iron phosphide. Particularly, FeP and Fe_2P phases were successfully demonstrated as efficient catalysts for NH_3 generation. Detection of the in-situ formed product was achieved using electrooxidation of NH_3 to nitrogen (N_2) on a Pt electrode. The Fe_2P catalyst exhibits the highest Faradaic efficiency (96%) for NH_3 generation with a yield (0.25 mmol h^{-1} cm^{-2} or 2.10 mg h^{-1} cm^{-2}) at −0.55 V vs. reversible hydrogen electrode (RHE). The recycling tests confirmed that Fe_2P and FeP catalysts exhibit excellent stability during the NO_3^- reduction at −0.37 V vs. RHE. To get relevant information about the reaction mechanisms and the fundamental origins behind the better

performance of Fe$_2$P, density functional theory (DFT) calculations were performed. These results indicate that the Fe$_2$P phase exhibits excellent performance to be deployed as an efficient noble metal-free catalyst for NH$_3$ generation.

Graphical abstract

Keywords:

iron phosphide, electrocatalysts, nitrates reduction, ammonia, DFT calculations

1. Introduction

Ammonia (NH$_3$) plays a crucial role in agriculture, pharmaceuticals, textile industry, and plastic production [1]. In addition, It is also considered an important energy storage medium and a promising carbon-free energy carrier because of its high content of hydrogen (17.6 wt %) [1]. The main industrial process for the synthesis of NH$_3$ is carried out through the reaction of nitrogen (N$_2$) and hydrogen (H$_2$) at elevated temperatures (400–500 °C) and pressures (150–300 atm) using the so-called Haber-Bosch process [2]. The latter method relies on the H$_2$ produced from fossil fuels and it requires intensive energy use leading to expensive operational costs [3]. In the past decade,

the electrochemical synthesis of NH_3 with renewable energy (wind or solar) input has attracted enormous interest as an alternative route [4]. Especially, the use of N_2 molecule in the electrochemical reduction process became a hot-topic [4]. While interesting progress in the development of N_2 reduction catalyst has been made, the low reaction rate of NH_3 evolution limits its widespread application [5,6]. The reduction of N_2 to NH_3 also suffers from low activity and selectivity due to the high stability of the triple non-polar bond ($N\equiv N$) [5]. Alternatively, the moderate dissociation energy of the $N=O$ bond (204 $kJmol^{-1}$) in nitrate ion (NO_3^-) makes it an attractive choice over N_2 since it promises better kinetics for NH_3 production [7,8]. Nitrates are common in nature in the form of metal nitrate deposits (e.g sodium nitrate ($NaNO_3$)) and they are considered one of the major surface and groundwater pollutants that are strictly regulated by environmental agencies due to their harmful effects [9]. NO_3^- source mainly comes from fertilizers, nuclear wastes, industrial wastewater, and livestock excrements with a wide range of concentrations up to ca. 2 M [4]. High levels of nitrate consumption may lead to serious immediate health problems (e.g. cancer) [10]. Because of this risk, the USEPA (U.S. Environmental Protection Agency) established that the maximum concentration of NO_3^- in water should not exceed 10 mg N/L [11]. Many common technologies were used to treat water contaminated with NO_3^- such as ion exchange, biological denitrification, and reverse osmosis [10]. Although, the ion exchange and the reverse osmosis are inapplicable for commercial applications because of the high cost of their additional pretreatment and posttreatment [12]. On the other hand, biological denitrification suffers from the slow potabilization system, and the risk of biological contamination since the process requires phosphorus resources and a certain amount of organic matrix, which can result in the generation of organic pollutants [12]. Using electrochemical methods to remove NO_3^- contaminants from wastewater has been an important and attractive topic in the environmental research field [4]. The efficient procedure of electrogenerated NH_3 from NO_3^- would serve dual purposes: First, for water purification, and second, for waste NO_3^- reuse to produce a highly useful chemical product (NH_3) [4]. Although the electrocatalytic nitrate reduction reaction (NO_3RR) is attractive, worth to mention that sometimes during NO_3RR may occur side reactions like the formation of products with low oxidation states such as nitrite (NO_2^-), nitrogen dioxide (NO_2), nitrous oxide (N_2O), nitric oxide (NO), hydrazine (NH_2NH_2), hydroxylamine (NH_2OH), etc [4,13]. For example, NH_2NH_2 and NH_2OH evolve preferably in acidic media, whereas NO_2^- and NH_3 are considered the main products in the neutral or basic environment [13]. Prior studies indicate that the transformation of NO_3^- into NO_2^- is the rate-determining step of NO_3RR [14]. Recently, the scientific focuses were mainly on obtaining highly active and selective catalysts for NO_3RR.

3

The activity of an electrocatalyst depends on various parameters such as medium pH, applied potential, surface area, crystal planes, composition, etc [15]. Mono metallic (Cu, Ru, etc.) and bimetallic (Pd−Cu, Pt−Cu, Pd−Sn, etc.) catalysts are among the most explored materials in electrocatalytic reduction of NO_3^- [16–20]. For example, Pt and Pd have been shown to exhibit a high activity toward NO_3^- reduction to NH_3 [20,21]. Another outstanding monometallic catalyst is the metal Ru. By using Ru clusters with internal strains, Yu et al. achieve 100% Faradaic efficiency (FE) for NO_3^- reduction. They claimed that strains in Ru clusters help the formation of hydrogen radicals, which accelerates the hydrogenation of NO_3^- during the reduction process [22]. In addition to monometallic nanoparticles (NPs), a bimetallic catalyst like CuPd has been proven to exhibit excellent performance for NO_3RR as well [14]. Although noble metals are efficient as catalysts, their high cost limits their widespread application. In addition to cost, an ideal catalyst for NO_3RR should offer good activity and selectivity [7]. Only recently, the development of low-cost catalysts which are selective for NO_3^- reduction gained interest. Zhang et al. demonstrated that oxygen vacancies in semiconductor TiO_2 electrodes improve the overall FE for NO_3^- reduction by weakening the N-O bond [3, 23]. Using metallic Cu NPs, Shih et al studied the impact of facets on the electrocatalytic NO_3^- reduction. The authors reported that different crystal facets contribute in different ways to the kinetics and the mode of electrocatalytic NO_3RR [24]. On the other hand, Sargent et al. have developed a Cu-Ni alloy catalyst with a unique electronic structure that has yielded a 6-fold increase in NO_3^- reduction activity compared to regular Cu electrodes [25]. Transition metal phosphides (TMPs) have emerged as promising low-cost candidates for electrocatalytic reduction reactions [26–30]. One of the most attractive features of TMPs is the charge transfer effect, $M(\delta^+) \rightarrow P(\delta^-)$, which allows reversibly to produce adsorbed hydrogen atoms (H) on the catalyst surface [26,30,31]. Moreover, TMPs have been developed because of their good conductivity due to d-electron configuration [32]. Recently, amorphous nickel phosphide (Ni_2P) deposited on carbon cloth was demonstrated as an efficient catalyst for NO_3RR [33]. Yao et al have developed a procedure to grow Ni_2P with (111) facet on Ni foam which yielded 0.056 mmol h^{-1} mg^{-1} NH_3 with FE equal to 99.2% [34]. Further, Yang et al also introduced Ni_2P catalyst for electrochemical NH_3 synthesis using NO_2^- as a source. Their catalyst showed a low onset potential of ~0.2 V vs. RHE with FE exceeding 90% [26, 35].

Herein, we report for the first time the NO_3RR to NH_3 using different phases of iron phosphide. We synthesized colloidal Fe_2P and FeP NPs and deposited them on a titanium (Ti) substrate by using a spin-coating approach. To activate the iron phosphide electrodes, a short heat treatment at 450 ºC was carried out. The Fe_2P catalyst showed the highest yield (0.25 mmol h^{-1} cm^{-2}) and FE

(96%) at -0.55 V vs. RHE for NH_3. Using NO_3^- as a starting species, we revealed the complex reaction pathways occurring during NH_3 generation. The recycling test confirmed that FeP catalysts exhibited excellent stability during the NO_3RR. To get relevant information about the fundamental origins behind the better performance of Fe_2P compared to FeP and to determine the free energies of intermediates, density functional theory (DFT) calculations were performed.

2. Experimental section

The preparation of Fe_2P and FeP was performed using a modified solvothermal synthesis procedure reported by chouki et al [36]. Details of the synthesis procedure and the experimental measurements can be found in Supporting Information (SI).

3. Results and discussion

3.1. Catalyst characterization

Following the activation of catalysts at 450 °C, we recorded the XRD pattern of iron phosphide samples (Fig. 1). The diffraction patterns are assigned to different phases: hexagonal for Fe_2P ($P\bar{6}2m$, PDF# 1008826) and orthorhombic for FeP (*Pbnm*, PDF# 9008932).
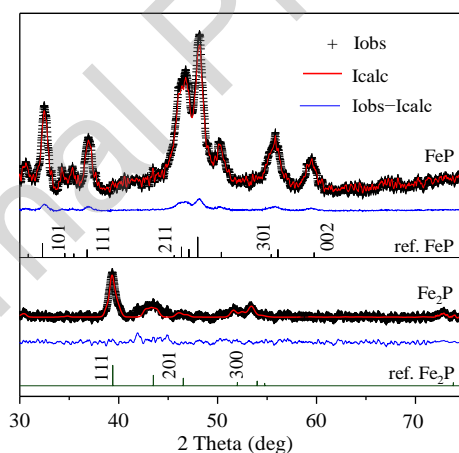

Fig. 1. XRD patterns of Fe_2P and FeP with Rietveld refinement fits. The blue lines show the difference between observed (symbol +) and calculated (red solid line) data. The XRD patterns of reference phases are given with labels.

The Rietveld refined crystal parameters for these phases gave: $a = b = 5.910 \pm 0.0070$ Å, and $c = 3.543 \pm 0.0040$ Å for Fe_2P, and $a = 3.105 \pm 0.0006$ Å, $b = 197 \pm 0.0004$ Å, and $c = 5.783 \pm 0.0007$ Å for FeP. These values are in good agreement with the literature [37]. The reliability of the refinement was assessed by the low values of the weighted profile (R_{wp}) factor, which is equal to $R_{wp} = 6.34\%$ for Fe_2P and $R_{wp} = 4.20\%$ for FeP. The processed data meet the established criteria ($R_{wp} < 20\%$) for good refinement [38].

5

Transmission electron microscopy (TEM) studies revealed that the FeP catalyst is composed of microsphere-like objects with typical sizes ranging from 400 to 1300 nm (Fig. 2a). Fig. 2c,d shows the uniform distribution of Fe and P elements (at.% ratio1:1) in the given agglomerate. The Fe_2P sample contained three types of particles: nanospheres (NSs), nanocubes (NCs), and nanorods (NRs) (Fig. 2f). While the Fe_2P NSs and Fe_2P NCs show uniform average diameters (8 ± 3.2 nm and 10 ± 2.3 nm), the Fe_2P NRs average sizes (7 ± 1.0 nm in diameter and 15 ± 2.7 nm in length) varies. High-resolution TEM (HR-TEM) studies indicated that the lattice spacing of 0.28 nm of the orthorhombic FeP (Fig. 2e) and 0.15 nm of the hexagonal Fe_2P (Fig. 2g) correspond respectively to the (200) and (102) crystal planes.

The morphology of Fe_2P and FeP thin films was studied using scanning electron microscopy (SEM). As can be seen from Fig. 2h, in the FeP film that is composed of microspheres, larger voids are formed. As determined from the cross-section SEM image, the thickness of the film is around ~26 μm (Fig. 2i). The Fe_2P thin film contains large aggregates (Fig. 2j) and densely packed NPs (Fig. 2k). The thickness of the Fe_2P film is about ~10 μm (Fig. 2l).
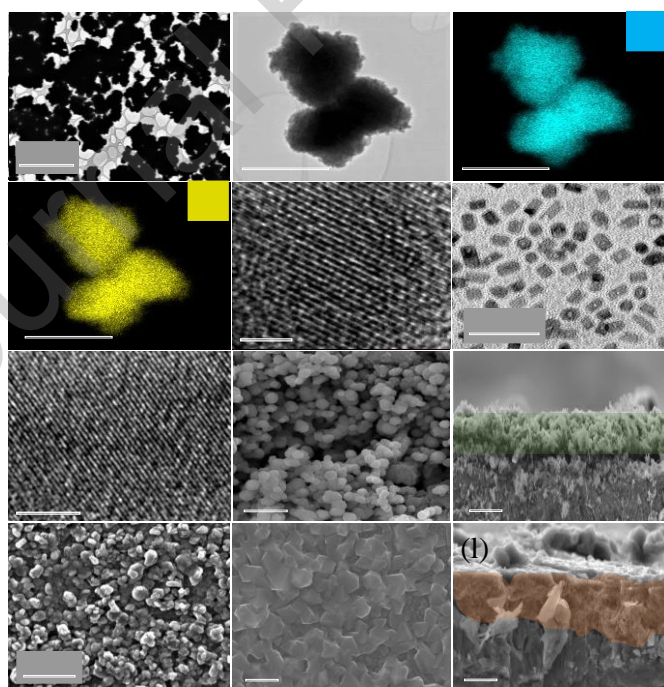

Fig. 2. TEM images of (a,b) FeP microspheres. EDX analysis of FeP taken from the image in (b) and its corresponding element maps of (c) Fe and (d) P. (e) HR-TEM image of FeP. In (f) is shown the TEM of Fe_2P NPs. (g) HR-TEM image taken from an individual Fe_2P NP. (h) SEM images of FeP microspheres recorded in top-view and (i) cross-section view of the Ti/FeP film. SEM images of densely packed Fe_2P NPs in (j,k) top-views and (l) cross-section view.

3.2. Electrochemical studies.

Electrocatalytic NO_3^- reduction experiments using iron phosphide films were performed in a mixture of 0.2 M $NaNO_3$ and 0.5 M sodium hydroxide (NaOH) at pH 13. The catalytic activities of Fe_2P and FeP catalysts for NO_3^- reduction were evaluated using the linear sweep voltammetry (LSV) method. LSV tests displayed that both catalysts have negligible electrochemical activity toward hydrogen evolution reaction (HER) in 0.5 M NaOH in the potential window from 0.0 to − 0.55 V vs RHE (Fig. 3a). To our expectation, the current density of Fe_2P and FeP cathodes were markedly increased upon adding $NaNO_3$ into the solution, which showed an onset potential at about −0.3 V vs. RHE for Fe_2P and −0.34 V vs. RHE for FeP. To explain the observed improved activities for NO_3RR we also conducted experiments using metallic iron (Fe) thin film. Fe is widely used for catalysis [39]. Recently, it was introduced as a good catalyst for NO_3^- reduction to NH_3 [4]. For comparison, we also provided LSV characteristics of Fe, iron oxide, Ti, Pt, and iron phosphate thin films. The LSV test showed that the Fe catalyst is not active for HER (Fig. S2). However, it showed a good activity toward NO_3^- reduction. It exhibited an onset potential at about −0.34 V vs. RHE which is comparable to FeP and Fe_2P catalysts (Fig. 3b). However, after repeated LSV cycles using Fe thin film the current greatly reduced which indicates an ongoing corrosion process (Fig. S2). Pt exhibited an onset potential at about −0.22 V vs. RHE which is lower than FeP and Fe_2P catalysts (Fig. S3). However, the high cost and scarcity of Pt limit its widespread use. On the other hand, Ti plate alone and pristine iron oxide deposited on Ti showed low current densities and high onset potentials > −0.4 V vs. RHE proving that they have negligible contributions to NO_3^- reduction (Fig. S3). It is noteworthy that the pristine iron phosphate thin film produced a lower current for NO_3^- reduction than the initial FeP and Fe_2P thin films. In addition, during the repetitive cyclic test, the activity of iron phosphate film decreased significantly which confirms once again its unsuitability for NO_3RR when is used as a stand alone film (Fig. S4). It seems that metal oxide and metal phosphate surface termination causes a synergistic effect which improves the activity of the iron phosphide films.

Tafel analysis was performed as a useful metric for interpreting the polarization curves [36, 40, 41]. Fig. 3c shows the Tafel relationships, potential versus $\log|j|$ (logarithm of current), for the HER and the NO_3RR recorded in 0.5 M NaOH and a mixture of 0.5 M NaOH / 0.2 M $NaNO_3$ (pH 13), respectively. The HER process usually goes through three reaction pathways: the Heyrovsky reaction (e.g. desorption step: H (ads) + H_3O^+ + e− → H_2 + H_2O), where H (ads) represents a hydrogen atom adsorbed at the active site of the catalyst), the Volmer reaction (e.g. discharge step: H_3O^+ + e− → H (ads) + H_2O, or the Tafel reaction (e.g.

discharge or recombination step: H (ads) + H (ads) → H$_2$). The Volmer reaction is considered slow since the adsorption of hydrogen on the active sites will result in a slope, higher than 116 mV dec^{-1} [41]. In the case of the NO$_3$RR, the reduction of nitrates proceeds according to the proposed mechanism: NO$_3^-$ (sol) ⇌ NO$_3^-$ (ads) and NO$^-$ (ads) + H (ads) + e− → NO$_2^-$ (ads) + OH$^-$. The produced NO$_2^-$ (ads) either desorbs from the surface of the electrode or reduces to give NH$_3$ according to the reaction: NO$_2^-$ (ads) + 5H (ads) + e− → NH$_3$ + 2OH$^-$ [42]. The obtained Tafel slopes using Fe$_2$P and FeP in 0.5 M NaOH were 184 mV dec^{-1} and 205 mV dec^{-1} respectively. The high Tafel slope values in 0.5 M NaOH suggest that the proton discharge is the rate-determining step on the surface of the catalysts [41]. However, the Tafel slopes decreased when we introduced NO$_3^-$ into the solution. The obtained values of 155 mV dec^{-1} for Fe$_2$P and 158 mV dec^{-1} for FeP reveal that the NO$_3$RR process follows a similar mechanism to that of Volmer-Heyrovsky where the Volmer reaction is the rate-limiting process. As expected, Ti showed the highest Tafel slope of 212 mV dec^{-1}. Since lower Tafel slope correlates to higher catalytic activity [36], the catalysts are ranked in the following order: Fe$_2$P > FeP > Ti.

Few catalysts are available for efficient NH$_3$ generation at low potentials. Recently, Wu et al. demonstrated the role of Fe single-atom catalyst (SAC) for NO$_3$RR. The authors showed that at −0.55 V vs RHE the Fe catalyst yielded a current density of 4.30 mA cm^{-2} which corresponds to 331 μg h^{-1} mg$_{cat.}^{-1}$ NH$_3$ yield at 39% FE [4]. Using CuO nanowire arrays, Zhang et al. demonstrated a more efficient NH$_3$ evolution process. However, they applied a very high potential (−0.85 V vs. RHE) to get 95.8% FE [1]. In our study, the applied potentials are under ≤ −0.55 V vs. RHE intending to suppress the competing HER process. Potentiostatic tests for NO$_3$RR at −0.50 V vs. RHE for three cycles revealed the stability of the electrodes (Fig. 3d). While the FeP shows decent current stability, the Fe$_2$P suffers from the decline of current which could be a sign of an ongoing corrosion process. During operation at high current densities, factors like internal resistance losses, accessibility of catalytic surfaces to reactants (liquid-solid-gas interfaces), electron transfer rate, and bonding strength may influence the catalyst performance [43].

LSVs were recorded to follow the activity of the iron phosphide films before and after the runs (Fig. S5). For the FeP catalyst, there is a slight drop in current. However, the onset potentials remained steady even after the third run. In the case of Fe$_2$P, both current and onset potential varied. To avoid corrosion of the film, the stability tests were also performed under

reduced applied potentials (−0.37 V vs. RHE). The results show that both films are stable in this case (Fig. S6).
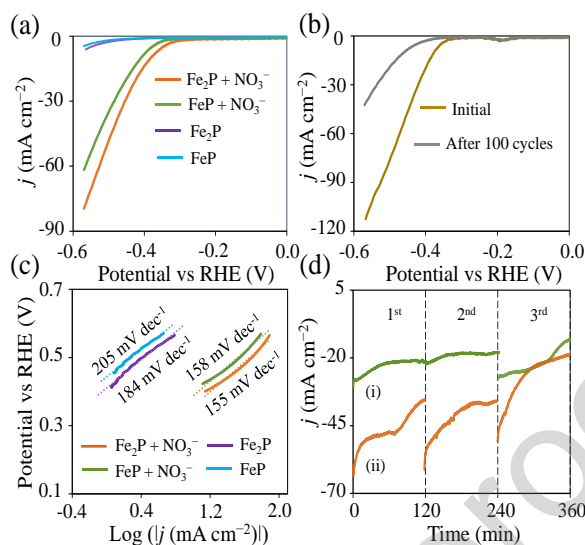

Fig. 3. (a) LSV characteristics of Fe_2P and FeP catalysts in 0.5 M NaOH and a mixture of 0.5 M NaOH / 0.2 M NO_3^- (pH 13) at 5 mV/s. (b) LSV characteristics of Fe catalyst recorded before and after 100 cycles. (c) Tafel slopes with and without NO_3^-. (d) Potentiostatic tests at −0.50 V vs. RHE for three cycles were recorded with (i) FeP and (ii) Fe_2P in the presence of NO_3^- ions.

Electrochemical impedance spectroscopy (EIS) was employed to measure the charge transfer resistance (R_{ct}) at the surface of electrocatalysts in a mixture of 0.5 M NaOH / 0.2 M $NaNO_3$ [44, 45]. Nyquist plots of Fe_2P and FeP films were recorded under applied potentials in the range from −0.1 to −0.6 V vs. RHE (Fig. 4a,b). The R_{ct} values were obtained after fitting the EIS data with the relevant circuits (Fig. S7a). The low R_{ct} values in the presence of NO_3^- are consistent with fast charge-transfer kinetics. The Ti was found to be active only in the potential range above −0.57 V vs. RHE. This result indicated that the Fe_2P and FeP catalysts have fast electron transfer and promising catalytic performance for NO_3^- reduction.

The detection of NH_3 has been identified electrochemically using FeP or Fe_2P as the working electrodes (2 cm^2 geometric area) following the long-term NO_3RR experiment under chronoamperometric conditions in deoxygenated 0.5 M NaOH / 0.2 M $NaNO_3$ solution. During the NO_3RR experiments, we used a bipotentiostate where one of them was attached to the iron phosphide working electrode which generated the NH_3 while the other was used for detection. The detection followed independent NH_3 oxidation using voltammetric diagnostic experiments in a manner analogous to that described previously for the detection of the CO_2 reduction products [46]. The analytical concept has been based on the previous observations postulating proportionality of the Pt-induced NH_3 oxidation currents on NH_3 concentration in the mM range [47]. Historically, electrooxidation of NH_3 attracted broad interest with respect

to wastewater treatment [48], and in NH_3 fuel cells [49, 50]. In this context, the concept of electrooxidation of NH_3 to N_2 has been widely explored despite the complexity of the mechanism for the oxidation of NH_3.

During NH_3 detection, the second working electrode modified with Pt catalytic NPs (deposited on glassy carbon) was placed in the vicinity of the FeP, or Fe_2P working electrode [51]. Fig. 4d illustrates the results of a series of blank NH_3 oxidation cyclic voltammetric (CV) experiments (curves a - d) performed in 0.5 M NaOH which contain intentionally added NH_3 in the concentration range from 1 to 10 mM.
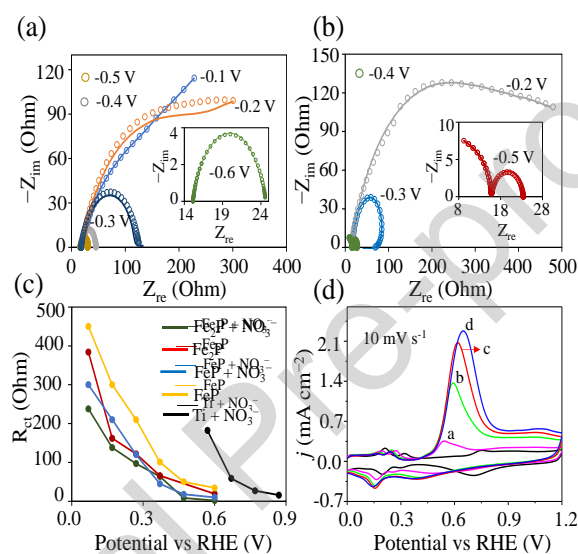

Fig. 4. EIS characteristics in a mixture of 0.2 M $NaNO_3$ and 0.5 M NaOH (pH 13) of (a) Fe_2P and (b) FeP. (c) Plot of R_{ct} vs. applied potential (negative values). (d) CV responses during the oxidation of NH_3 at (a) 1, (b) 5, (c) 8, and (d) 10 mM using Pt decorated working electrode. The dark line illustrates the response recorded in the NH_3-free solution.

Single voltammetric peaks of NH_3 oxidation have emerged at potentials ranging from 0.55 to 0.70 V vs. RHE. Although the peak potentials are somewhat concentration-dependent, the voltammetric peak responses are well-defined. The black line stands for the typical response of Pt NPs in NH_3-free alkaline (0.5 M NaOH) medium [52]. Here, in the potential range from 0.0 to 0.4 V vs. RHE, hydrogen adsorption peaks are developed and at potentials higher than 0.7 V vs. RHE, the reversible oxidation of platinum to platinum oxides has been observed. In between the hydrogen peaks and formation of Pt oxides, platinum exists mostly in the metallic form. It is apparent from Fig. 4d (curves a – d) that the oxidation of NH_3 to N_2 is catalyzed by metallic platinum, rather than Pt oxides (evident from the decrease of the oxidation currents at/above 0.8 V vs. RHE). The proportionality of the peak-current densities on NH_3 concentration is evident from the Fig. S7b. Since the Fe_2P film gave the highest

10

NO$_3$RR current densities (relative to FeP) our discussion will be mainly on Fe$_2$P (Fig. S8). The long-term (2 h) chronoamperometric reduction of NO$_3^-$ has been performed (at the Fe$_2$P working electrode) in a two-chamber electrolytic cell (subjected to continuous saturation with argon) upon application of −0.55 V vs. RHE (Fig. S8).

By comparing the net voltammetric peak-current density (Fig. S9a) with the analogous current density values originating from blank experiments at different concentrations (working curve in the Fig. S7b), the NH$_3$ concentration generated following the NO$_3$RR at the Fe$_2$P electrode upon application of –0.55 V vs. RHE has been estimated to be equal to 4.7 mM. Judging from the amount of charge (188 C cm^{-2}) transferred during the electrolysis for 7200 s at the 2 cm^2 Fe$_2$P-electrode (Fig. S8a), and by assuming 100% efficiency of the 8-electron reduction of NO$_3^-$ to NH$_3$, the NH$_3$ concentration equal to 4.9 mM has been obtained. By comparing the above concentration values 4.7 and 4.9, the FE toward the production of NH$_3$ can be postulated to be on the level of 96%.

The appearance of a single peak in the voltammogram supports our view that NH$_3$ is the main N$_2$ reaction product (Fig. S9a). In particular, no NH$_2$NH$_2$ is expected to be formed here because its oxidation peak on platinum would appear at less positive potentials, namely starting from 0.2 V vs. RHE [53], which is not the case in this study. The fact that some current increase is observed at potentials higher than 0.8 V vs. RHE should be attributed to the system's further oxidation, namely to the oxidation of N$_2$-product to nitrogen oxo species [54]. This "tailing effect" observed at positive potentials does not seem to interfere with the analytical diagnosis based on the determination of the peak current density (Fig. S9a). Any formation of sizeable amounts of NO$_2^-$ and nitrogen oxides (N$_2$O, NO, N$_2$O$_3$, etc.) [54] would result in the sizeable reduction peak currents at about 0.2 V vs. RHE in the reduction voltammetric scans. As demonstrated during voltammetric diagnostic experiments in solutions containing the intentionally introduced NO$_2^-$ at various concentrations (Fig. S9b). No such responses have been obtained in the analyzed solutions after electrolysis at −0.55 V vs. RHE. Because our present results are consistent with the view that NH$_3$, together with hydrogen, are generated at Fe$_2$P during NO$_3$RR, estimation of the selectivity efficiency has also been based on this assumption. Remembering that formation of H$_2$ is the two-electron reaction, and conversion of NO$_3^-$ to NH$_3$ is the eight-electron process, it can be rationalized from the 96% FE (calculated for the NH$_3$ generation) that the selectivity (molar) efficiency is equal to ca. 84%. To validate this result, some attention has been paid to the dynamics of hydrogen evolution in the NH$_3$-containing NaOH. Thus, we have performed an additional

chronoamperometric experiment in 0.5 M NaOH containing 4.6 mM NH_3, namely, to simulate hydrogen evolution in the presence of NH_3 generated during NO_3^- reduction in an alkaline medium. Inset b of Fig. S8 shows that the addition of NH_3 tends to decrease hydrogen evolution (dashed line), relative to the performance at NH_3 free conditions (solid line). Based on the comparison of the H_2-evolution current (after 1000 s from the dashed line in Fig. S8b) and the current recorded after 1000 s during NO_3RR electrolysis, as well as remembering that different numbers of electrons are involved in both processes, the selectivity (molar) efficiency can be estimated to be on the level 80%. The obtained values, 80 and 84% are comparable, and the difference between them may reflect the uncertainty in the assumption about the hydrogen evolution efficiency in the presence of NH_3 formed during the NO_3RR electrolysis. At −0.55 V vs. RHE, the Fe_2P catalyst has exhibited 0.25 mmol h^{-1} cm^{-2} or 2.10 mg h^{-1} cm^{-2} reaction rates toward NH_3 generation. Upon application of less negative potentials, −0.50 and −0.37 V vs. RHE, the yields have been lower, 1.50 mg h^{-1} cm^{-2} and 0.42 mg h^{-1} cm^{-2}, respectively. While the FeP catalyst has also been characterized by the comparably high FE of 94% for NH_3 generation at −0.55 V vs. RHE, the reaction rate has been found under such conditions to be lower (0.12 mmol h^{-1} cm^{-2} or 1.0 mg h^{-1} cm^{-2}), when compared to the performance of Fe_2P. Upon application of less negative potentials to FeP, −0.50 and −0.37 V vs. RHE, the reaction rates have been rather low, 0.71 and 0.19 mg h^{-1} cm^{-2}, respectively. The obtained yields at −0.55 V vs. RHE using the active Fe_2P phase were found to be higher or comparable to what is reported in the literature (Table S1).

To validate the formation of NH_3 during the electrochemical NO_3RR mass spectrometry (MS) analysis was used as another proof (Fig. S10). The sudden rise of ionic current at 28 s indicates the presence of fragment ions with a mass-to-charge ratio equal to $m/z = 17$ for NH_3. In addition, the absence of H_2 ($m/z = 2$) during NO_3RR suggests that HER is suppressed during NH_3 production.

Fourier transform infrared (FTIR) was used to identify the characteristic vibration components present in the FeP and Fe_2P samples (Fig. 5a,b). The C-H bending vibration at 3000 cm^{-1} which comes from surface passivated organics is present in FeP and Fe_2P samples [55]. Similarly, the intensive band at 1740 cm^{-1} in FeP and 1730 cm^{-1} in Fe_2P samples are attributed to the bending vibrations of C=O bonds [56, 57]. Stretching vibrations of -CH_3 are assigned to the bands at 1352 and 1455 cm^{-1} in the Fe_2P sample [58]. In the case of the FeP, the CH_3 band is located at around 1371 cm^{-1} [59, 60]. The bands located at 1086 cm^{-1} (FeP) and 850 cm^{-1} (Fe_2P) confirm the presence of phosphate (P-O) species [61, 62]. Comparison of

FTIR spectra recorded from the FeP film before and after the stability tests shows insignificant changes. However, in the case of Fe_2P, the intensity of the P-O peaks dramatically decreased after the test, which confirms the masking or leaching of phosphorus during the NO_3RR. The composition and the chemical state of FeP and Fe_2P thin films were characterized by XPS. The XPS survey spectrum of the FeP and Fe_2P electrodes before and after NO_3^- reduction is shown in Fig. 5c,d. XPS narrow scans of Fe 2p, O 1s, and P 2p regions recorded from the FeP sample (before the NO_3^- reduction) are shown in Fig. 6a,c and e. The spectrum of Fe 2p displays characteristic peaks at 711.4 and 725.0 eV, corresponding to $2p^{3/2}$ and $2p^{1/2}$ levels of Fe^{2+} [63]. The positions of the peaks suggest that Fe appears in the form of iron oxide and iron phosphate (major phase) [64]. The peaks at 715.0 and 729.8 eV are assigned to Fe^{3+}, indicating the coexistence of Fe^{3+} and Fe^{2+} in the FeP sample. The peaks at 719.2 and 734.3 eV are satellite peaks, which belong to Fe $2p^{3/2}$ and Fe $2p^{1/2}$, respectively [63]. The characteristic O 1s line shows an intensive broad signal which contains several individual peaks. The peak at 530.4 eV confirms the divalent valence state of O in the FeP. The other two peaks at 531.6 and 533.4 eV are attributed to the C–O and C=O bands arising from functional groups absorbed on the sample surface [65]. The three signals within the P 2p envelope of FeP are attributed to surface oxidized P species and P from the iron phosphide [64]. The two peaks at 134.0 and 133.3 eV could be from the PO_4^{3-} or P_2O_5 due to the unavoidable oxidation of P species either during the synthesis or heat-treatment process. The peak at 130.8 eV reflects the binding energy of P 2p1/2 which can be assigned to P bonding to Fe. Selected regions of the XPS spectra of Fe_2P recorded before NO_3^- reduction are shown in Fig. 6g,i and k. The photoelectron Fe 2p signal exhibits a doublet at 711.4 eV (Fe $2p_{3/2}$) and 724.8 eV (Fe $2p_{1/2}$) due to spin-orbit splitting. These peaks can be attributed to the oxidized state of Fe formed on the Fe_2P surface, demonstrating the oxidation state of Fe^{2+} [64, 66]. A small peak at 714.8 is assigned to $Fe^{3+,}$ indicating the coexistence of Fe^{3+} and Fe^{2+} in the Fe_2P sample [63]. The O 1s shows a peak at 530.3 eV, confirming that the valence state of O is divalent (Fe-O, metal-containing oxygen bond). The two shoulder peaks at 531.8 and 533.6 eV are attributed to the C–O and C=O bands arising from molecules absorbed on the sample surface [65]. The P 2p signal in the Fe_2P sample is almost missing which can be explained by the fact that oxide-rich iron phosphate forms on the Fe_2P surface and masks the signal of P 2p [67, 68].
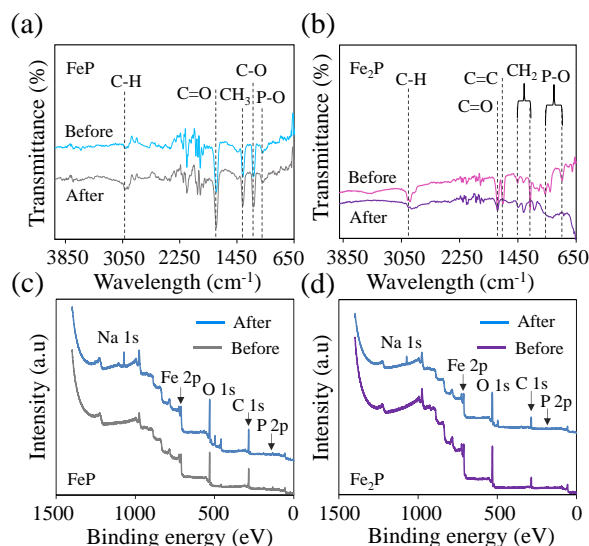
Fig. 5. (a-b) FTIR spectra and (c-d) XPS survey scans of FeP and Fe$_2$P taken before and after the NO$_3$RR tests.

To gain a better understanding of Fe$_2$P and FeP catalyst surface chemistry, we also recorded XPS spectra after the NO$_3^-$ reduction test (Fig. 6). The results of the quantitative analysis of the XPS are shown in detail in Table S2 and Table S3. The XPS peak intensities can be converted to atomic concentrations (at %) using the sensitivity factors determined experimentally or simply calculated [69]. For the Fe$_2$P sample, the atomic and the mass concentration (mass %) of Fe 2p, O 1s, and Ti 2p before and after the test did not show any drastic changes. However, the analysis shows that P 2p decreased more than 3 times after the test. The at % of P 2p decreased from 4.71 to 1.19 %. In the case of FeP, the at % of Fe 2p increased from 13.99 to 27.35. On the other side, the at % of P 2p decreased from 15.27 to 2.892. The extensive decrease of P 2p is explained by the fact that phosphorus transformed to phosphate (hidden by surface oxygen species) or consumed due to corrosion during the reduction of NO$_3^-$.
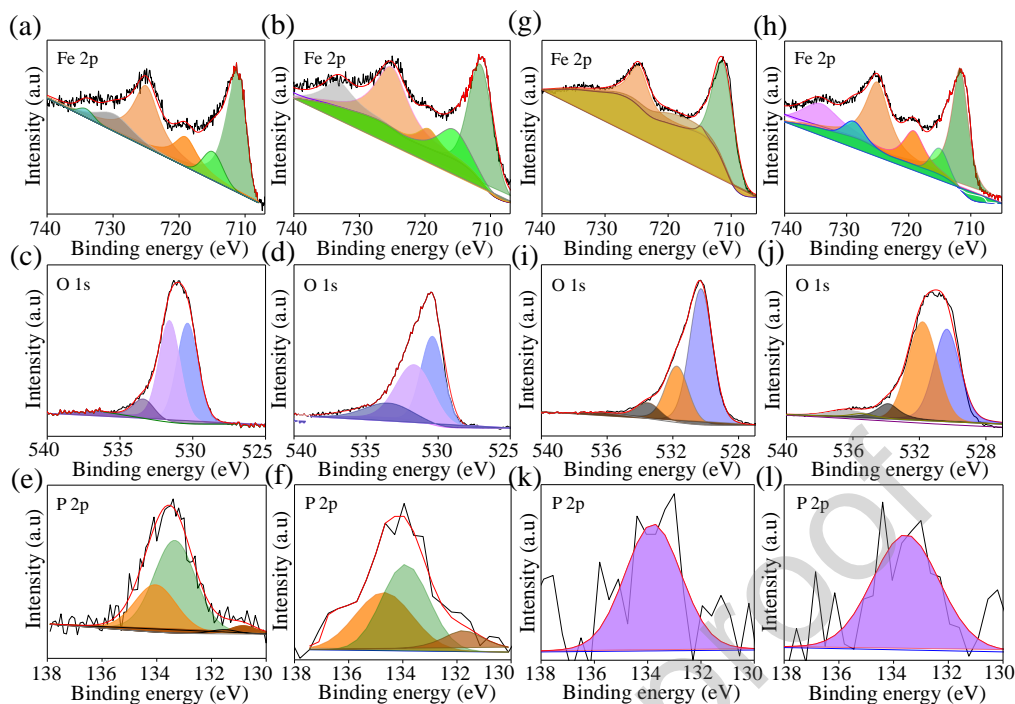
Fig. 6. XPS core-level spectra of FeP recorded before (a,c,e) and after (b,d,f) the test. The characteristic lines of Fe$_2$P before (g,i,k) and after (h,j,l) the stability studies.

3.3.   Reaction mechanism.

The reaction mechanism for NO$_3$RR catalyzed by Fe$_2$P and FeP electrocatalysts has been studied using DFT at the RPBE+D3 level of theory in an aqueous solution. Our models have been constructed based on the intensities of the XRD patterns (Fig. 1) and XPS data analysis, leading to the building of the oxidized Fe$_2$P (111) and phosphate-coated FeP (101) surfaces (see Fig. S12). These are also characterized by the presence of a vacancy that will act as an active site where the substrates will interact with the catalytic surface along the NO$_3$RR. The reduction of NO$_3^-$ into NH$_3$ entails the transfer of nine protons and eight electrons, however, with the assumption that both NO$_3^-$ and its protonated form of nitric acid (HNO$_3$) are in equilibrium, the modeling focuses on the study of the HNO$_3$ adsorption and NH$_3$ desorption phenomena as the initial and final steps to the global process defined by the electrochemical equation HNO$_3$ (ac) + 8 H$^+$ + 8 e^- $\rightleftharpoons$ NH$_3$ (ac) + 3 H$_2$O (l). In this context, Fig. 7 gathers the structures of each elementary reaction step and the free energies associated with each one at room temperature and pressure conditions when there is no applied potential ($U = 0$) and pH = 14 (basic). Interestingly, both the oxidized Fe$_2$P (111) and phosphate-coated FeP (101) surfaces present spontaneous binding free energies for HNO$_3$ adsorption, –0.34 and –0.51 eV, respectively. This fact is due to the presence of low-coordinated surface Fe atoms, specifically three-fold (3c), making them electrophilic and therefore expecting greater interactions with

15

the substrates than other surfaces constituted by higher coordinated surface Fe atoms (see Fig. S13). Both, the oxidized Fe_2P (111) and phosphate-coated FeP (101) surfaces present similar catalytic profiles for the first four reduction steps, that is, the formation of $*NO_2$, $*HNO_2$, $*NO$, and $*NOH$ intermediate species (see Fig. 7, more details at Fig. S15).
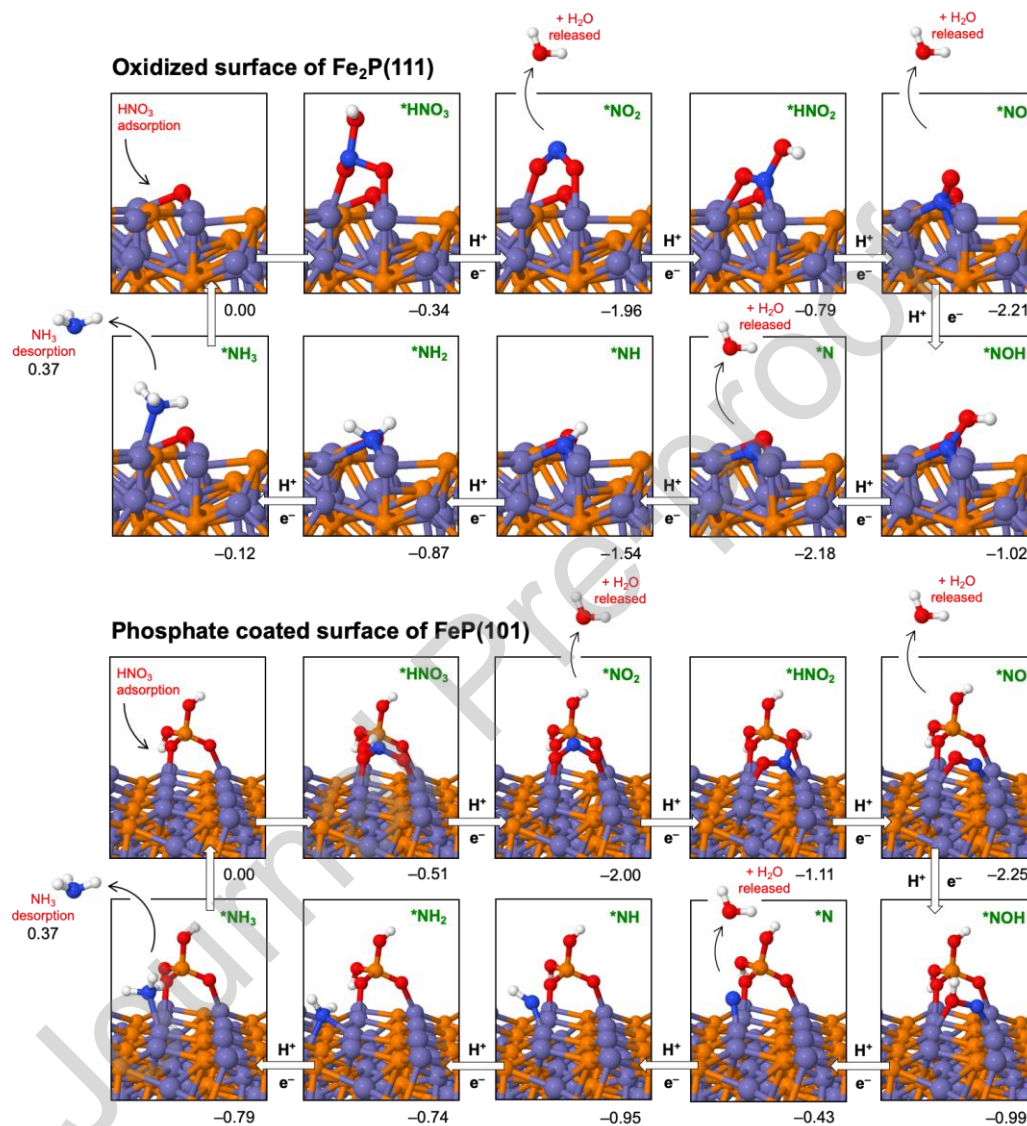

Fig. 7. Proposed reaction mechanism for the electrochemical HNO_3 conversion into NH_3 (NO_3RR) catalyzed by the oxidized Fe_2P (111) (top) and phosphate coated FeP (101) (bottom) surfaces. Reaction-free energies at room temperature are shown in eV when there is no applied potential ($U = 0$) and pH = 14.

Both the production of NO_2 and NO are spontaneous processes with –1.62 and –1.42 eV for Fe_2P (111) and –1.49 and –1.14 eV for FeP (101), expected values given the great potential of these species to coordinate with metal centers. With a contrary trend, the formation of nitrous acid and nitroxyl is non-spontaneous with values of 1.17 and 1.19 eV for Fe_2P (111) and 0.89 and 1.26 eV for FeP (101). This last, that is, the nitroxyl formation as a

consequence of the fourth hydrogenation, $*NO + H^+/e^- \rightleftharpoons *NOH$, represents the step with the highest thermodynamics impediment, expecting a maximum overpotential of –1.19 and –1.26 V vs. CHE (computational hydrogen electrode) equivalent to the SHE, or –0.36 and –0.43 V vs. RHE (pH = 14) for Fe_2P (111) and FeP (101), respectively. Interestingly, our calculations estimate values of anodic potentials very close to those observed experimentally, validating the construction of our models. Up to this point, all substrates interact with the Fe_2P (111) and FeP (101) surfaces through, at least, two binding points involving the two three-coordinated surface Fe atoms. A greater distance of them in the FeP (101) makes the metal nitride species and its subsequent hydrogenated amino $*NH$ and $*NH_2$ intermediates less stabilized than the ones on the Fe_2P (111) surface. Finally, the NH_3 desorption is calculated as just 0.49 eV for the oxidized Fe_2P (111) surface while for the phosphate-coated FeP (101) one a heavy value of 1.15 eV is observed, indicating a possible catalyst poisoning for this second case.

4. Conclusion

In this work, we report the use of iron phosphides as highly efficient noble metal-free catalysts in NO_3RR studies. A modified solvothermal synthesis procedure using triphenylphosphine precursor was used to prepare the Fe_2P and FeP catalysts. Impressively, the Fe_2P catalyst shows the highest FE (96%) and yield (2.10 mg h^{-1} cm^{-2}) at −0.55 V vs. RHE for NH_3 generation. For the FeP catalyst, at−0.50 and −0.37 V vs. RHE, the yields were found to be 0.71 mg h^{-1} cm^{-2} and 0.19 mg h^{-1} cm^{-2}, respectively. The recycling test confirmed that both FeP and Fe_2P catalysts exhibited excellent stability during the NO_3RR at −0.37 V vs. RHE. Herein, the reported catalytic activities also consider the presence of metal oxide and metal phosphate surface terminations, which contributes in a synergistic way to the observed enhanced activities of iron phosphide films. DFT calculations supported the experimental observations and explained the mechanism and the fundamental origins behind the better performance of Fe_2P as compared to FeP. This study demonstrates the tremendous potential of iron phosphide catalysts as efficient cathodes toward NO_3RR to NH_3. Hence, this work could be also extended to other TMPs for selectively converting different nitrogen oxides into valuable green NH_3 under benign conditions.

CRediT authorship contribution statement

T. Chouki: designed and conducted the experiments, analyzed the data and wrote the manuscript. **M. Machreki:** contributed to EIS measurements. **I. A. Rutkowska** and **B. Rytelewska:** contributed to electrochemical tests. **P. J. Kulesza:** contributed to

electrochemical tests, data analysis, fund-raising, and project administration. **G. Tyuliev:** carried out the XPS measurements. **M. Harb** and **L. Miguel Azofra:** carried out the DFT calculations. **S. Emin:** supervised the work, and contributed to data analysis, manuscript writing and editing, fund-raising, and project administration.

Declaration of interests

☒ The authors declare that they have no known competing financial interests or personal relationships that could have appeared to influence the work reported in this paper.

☐ The authors declare the following financial interests/personal relationships which may be considered as potential competing interests:

Acknowledgments

Declaration of Competing Interest

The authors declare that they have no known competing financial interests or personal relationships that could have appeared to influence the work reported in this paper.

References

[1]   Y. Wang, W. Zhou, R. Jia, Y. Yu, B. Zhang, Unveiling the activity origin of a copper-based electrocatalyst for selective nitrate reduction to ammonia, Angew. Chemie - Int. Ed. 59 (2020) 5350–5354. https://doi.org/10.1002/anie.201915992.

[2]   B.H.R. Suryanto, H.L. Du, D. Wang, J. Chen, A.N. Simonov, D.R. MacFarlane, Challenges and prospects in the catalysis of electroreduction of nitrogen to ammonia, Nat. Catal. 2 (2019) 290–296. https://doi.org/10.1038/s41929-019-0252-4.

[3]   P.H. van Langevelde, I. Katsounaros, M.T.M. Koper, Electrocatalytic nitrate reduction for sustainable ammonia production, Joule. 5 (2021) 290–294. https://doi.org/10.1016/j.joule.2020.12.025.

[4]   Z.Y. Wu, M. Karamad, X. Yong, Q. Huang, D.A. Cullen, P. Zhu, C. Xia, Q. Xiao, M. Shakouri, F.Y. Chen, J.Y. (T) Kim, Y. Xia, K. Heck, Y. Hu, M.S. Wong, Q. Li, I. Gates, S. Siahrostami, H. Wang, Electrochemical ammonia synthesis via nitrate reduction on Fe single atom catalyst, Nat. Commun. 12 (2021) 1–10. https://doi.org/10.1038/s41467-021-23115-x.

[5]   C. Tang, S.Z. Qiao, How to explore ambient electrocatalytic nitrogen reduction reliably and insightfully, Chem. Soc. Rev. 48 (2019) 3166–3180. https://doi.org/10.1039/c9cs00280d.

[6]   P. Chen, N. Zhang, S. Wang, T. Zhou, Y. Tong, C. Ao, W. Yan, L. Zhang, W. Chu, C. Wu, Y. Xie, Interfacial engineering of cobalt sulfide/graphene hybrids for highly efficient ammonia electrosynthesis, Proc. Natl. Acad. Sci. U. S. A. 116 (2019) 6635–6640. https://doi.org/10.1073/pnas.1817881116.

[7]   G.F. Chen, Y. Yuan, H. Jiang, S.Y. Ren, L.X. Ding, L. Ma, T. Wu, J. Lu, H. Wang, Electrochemical reduction of nitrate to ammonia via direct eight-electron transfer using a copper–molecular solid catalyst, Nat. Energy. 5 (2020) 605–613. https://doi.org/10.1038/s41560-020-0654-1.

[8]   Q. Hu, Y. Qin, X. Wang, H. Zheng, K. Gao, H. Yang, P. Zhang, M. Shao, C. He, Grain boundaries engineering of hollow copper nanoparticles enables highly efficient ammonia electrosynthesis from nitrate, CCS Chem. 4 (2022) 2053–2064. https://doi.org/10.31635/ccschem.021.202101042.

[9]   S. Hamid, Y. Niaz, S. Bae, W. Lee, Support induced influence on the reactivity and selectivity of nitrate reduction by Sn-Pd bimetallic catalysts, J. Environ. Chem. Eng. 8 (2020) 103754. https://doi.org/10.1016/j.jece.2020.103754.

[10]   G. Mendow, N.S. Veizaga, C.A. Querini, B.S. Sánchez, A continuous process for the catalytic reduction of water nitrate, J. Environ. Chem. Eng. 7 (2019) 102808. https://doi.org/10.1016/j.jece.2018.11.052.

[11]   F.A. Marchesini, V. Aghemo, I. Moreno, N. Navascués, S. Irusta, L. Gutierrez, Pd and Pd,In nanoparticles supported on polymer fibres as catalysts for the nitrate and nitrite reduction in aqueous media, J. Environ. Chem. Eng. 8 (2020) 103651.

https://doi.org/10.1016/j.jece.2019.103651.

[12] Q. Niu, S. Yang, Z. Song, C. Liu, Z. Li, X. Wang, L. Song, Fabrication of efficient and robust Fe^0/Ni$_2$P/CC composite and the employment for electrochemical reduction of nitrate, J. Environ. Chem. Eng. 9 (2021) 106412. https://doi.org/10.1016/j.jece.2021.106412.

[13] I. Katsounaros, D. Ipsakis, C. Polatides, G. Kyriacou, Efficient electrochemical reduction of nitrate to nitrogen on tin cathode at very high cathodic potentials, Electrochim. Acta. 52 (2006) 1329–1338. https://doi.org/10.1016/j.electacta.2006.07.034.

[14] H. Xu, J. Wu, W. Luo, Q. Li, W. Zhang, J. Yang, Dendritic cell-inspired designed architectures toward highly efficient electrocatalysts for nitrate reduction reaction, Small. 16 (2020) 1–16. https://doi.org/10.1002/smll.202001775.

[15] I.- Ul-Haque, M. Tariq, Electrochemical reduction of nitrate: A review, J. Chem. Soc. Pakistan. 32 (2010) 396–418.

[16] E. Pérez-Gallent, M.C. Figueiredo, I. Katsounaros, M.T.M. Koper, Electrocatalytic reduction of nitrate on copper single crystals in acidic and alkaline solutions., Electrochim. Acta. 227 (2017) 77–84. https://doi.org/10.1016/j.electacta.2016.12.147.

[17] B.P. Chaplin, J.R. Shapley, Regeneration of sulfur-fouled bimetallic Pd-based catalysts, Environ. Sci. Technol. 41 (2007) 5491–5497. https://doi.org/10.1021/es0704333.

[18] S.E. Bae, K.L. Stewart, A.A. Gewirth, Nitrate adsorption and reduction on Cu(100) in acidic solution, J. Am. Chem. Soc. 129 (2007) 10171–10180. https://doi.org/10.1021/ja071330n.

[19] L. Szpyrkowicz, S. Daniele, M. Radaelli, S. Specchia, Removal of NO$_3^-$ from water by electrochemical reduction in different reactor configurations, Appl. Catal. B Environ. 66 (2006) 40–50. https://doi.org/10.1016/j.apcatb.2006.02.020.

[20] J.F.E. Gootzen, P.G.J.M. Peeters, J.M.B. Dukers, L. Lefferts, W. Visscher, J.A.R. Van Veen, The electrocatalytic reduction of NO$_3^-$ on Pt, Pd and Pt + Pd electrodes activated with Ge, J. Electroanal. Chem. 434 (1997) 171–183. https://doi.org/10.1016/S0022-0728(97)00093-4.

[21] A. Pintar, J. Batista, I. Muševič, Palladium-copper and palladium-tin catalysts in the liquid phase nitrate hydrogenation in a batch-recycle reactor, Appl. Catal. B Environ. 52 (2004) 49–60. https://doi.org/10.1016/j.apcatb.2004.02.019.

[22] J. Li, G. Zhan, J. Yang, F. Quan, C. Mao, Y. Liu, B. Wang, F. Lei, L. Li, A.W.M. Chan, L. Xu, Y. Shi, Y. Du, W. Hao, P.K. Wong, J. Wang, S.X. Dou, L. Zhang, J.C. Yu, Efficient ammonia electrosynthesis from nitrate on strained ruthenium nanoclusters, J. Am. Chem. Soc. 142 (2020) 7036–7046. https://doi.org/10.1021/jacs.0c00418.

[23] R. Jia, Y. Wang, C. Wang, Y. Ling, Y. Yu, B. Zhang, Boosting selective nitrate electroreduction to ammonium by constructing oxygen vacancies in TiO$_2$, ACS Catal. 10 (2020) 3533–3540. https://doi.org/10.1021/acscatal.9b05260.

[24] Y.J. Shih, Z.L. Wu, Y.H. Huang, C.P. Huang, Electrochemical nitrate reduction as affected by the crystal morphology and facet of copper nanoparticles supported on nickel foam electrodes

(Cu/Ni), Chem. Eng. J. 383 (2020) 123157. https://doi.org/10.1016/j.cej.2019.123157.

[25]   Y. Wang, A. Xu, Z. Wang, L. Huang, J. Li, F. Li, J. Wicks, M. Luo, D.H. Nam, C.S. Tan, Y. Ding, J. Wu, Y. Lum, C.T. Dinh, D. Sinton, G. Zheng, E.H. Sargent, Enhanced nitrate-to-ammonia activity on copper-nickel alloys via tuning of intermediate adsorption, J. Am. Chem. Soc. 142 (2020) 5702–5708. https://doi.org/10.1021/jacs.9b13347.

[26]   X. Yang, L. Kang, C.-J. Wang, F. Liu, Y. Chen, Electrochemical ammonia synthesis from nitrite assisted by in situ generated hydrogen atoms on a nickel phosphide catalyst, Chem. Commun. 57 (2021) 7176–7179. https://doi.org/10.1039/d1cc02410h.

[27]   T. Liu, A. Li, C. Wang, W. Zhou, S. Liu, L. Guo, Interfacial electron transfer of Ni_2P–NiP_2 Polymorphs inducing enhanced electrochemical properties, Adv. Mater. 30 (2018) 1–9. https://doi.org/10.1002/adma.201803590.

[28]   E.J. Popczun, J.R. McKone, C.G. Read, A.J. Biacchi, A.M. Wiltrout, N.S. Lewis, R.E. Schaak, Nanostructured nickel phosphide as an electrocatalyst for the hydrogen evolution reaction, J. Am. Chem. Soc. 135 (2013) 9267–9270. https://doi.org/10.1021/ja403440e.

[29]   E.J. Roberts, C.G. Read, N.S. Lewis, R.L. Brutchey, Phase directing ability of an ionic liquid solvent for the synthesis of HER-active Ni_2P nanocrystals, ACS Appl. Energy Mater. 1 (2018) 1823–1827. https://doi.org/10.1021/acsaem.8b00213.

[30]   P. Liu, J.A. Rodriguez, Catalysts for hydrogen evolution from the [NiFe] hydrogenase to the $Ni_2P(001)$ surface: The importance of ensemble effect, J. Am. Chem. Soc. 127 (2005) 14871–14878. https://doi.org/10.1021/ja0540019.

[31]   P. Liu, J.A. Rodriguez, T. Asakura, J. Gomes, K. Nakamura, Desulfurization reactions on $Ni_2P(001)$ and α-$Mo_2C(001)$ surfaces: Complex role of P and C sites, J. Phys. Chem. B. 109 (2005) 4575–4583. https://doi.org/10.1021/jp044301x.

[32]   T. Zhao, Y. Wang, S. Karuturi, K. Catchpole, Q. Zhang, C. Zhao, Design and operando/in situ characterization of precious-metal-free electrocatalysts for alkaline water splitting, Carbon Energy. 2 (2020) 582–613. https://doi.org/10.1002/cey2.79.

[33]   S. Huo, S. Yang, Q. Niu, F. Yang, L. Song, Synthesis of functional Ni_2P/CC catalyst and the robust performances in hydrogen evolution reaction and nitrate reduction, Int. J. Hydrogen Energy. 45 (2020) 4015–4025. https://doi.org/10.1016/j.ijhydene.2019.11.210.

[34]   Q. Yao, J. Chen, S. Xiao, Y. Zhang, X. Zhou, Selective electrocatalytic reduction of nitrate to ammonia with nickel phosphide, ACS Appl. Mater. Interfaces. 13 (2021) 30458–30467. https://doi.org/10.1021/acsami.0c22338.

[35]   X. Fan, L. Xie, J. Liang, Y. Ren, L. Zhang, L. Yue, T. Li, Y. Luo, N. Li, B. Tang, Y. Liu, S. Gao, A.A. Alshehri, Q. Liu, Q. Kong, X. Sun, In situ grown Fe_3O_4 particle on stainless steel: A highly efficient electrocatalyst for nitrate reduction to ammonia, Nano Res. 15 (2021) 3050–3055. https://doi.org/10.1007/s12274-021-3951-5.

[36]   T. Chouki, M. Machreki, S. Emin, Solvothermal synthesis of iron phosphides and their

application for efficient electrocatalytic hydrogen evolution, Int. J. Hydrogen Energy. 45 (2020) 21473–21482. https://doi.org/10.1016/j.ijhydene.2020.05.257.

[37] J. Park, B. Koo, Y. Hwang, C. Bae, K. An, J.G. Park, H.M. Park, T. Hyeon, Novel synthesis of magnetic Fe_2P nanorods from thermal decomposition of continuously delivered precursors using a syringe pump, Angew. Chemie - Int. Ed. 43 (2004) 2282–2285. https://doi.org/10.1002/anie.200353562.

[38] A. Rasras, R. Hamdi, S. Mansour, A. Samara, Y. Haik, Study of the magnetocaloric effect in single-phase antiferromagnetic $GdMnO_3$, J. Phys. Chem. Solids. 149 (2021) 109798. https://doi.org/10.1016/j.jpcs.2020.109798.

[39] W. Da Oh, Z. Dong, T.T. Lim, Generation of sulfate radical through heterogeneous catalysis for organic contaminants removal: Current development, challenges and prospects, Appl. Catal. B Environ. 194 (2016) 169–201. https://doi.org/10.1016/j.apcatb.2016.04.003.

[40] T. Chouki, D. Lazarević, B. V. Donkova, S. Emin, Synthesis of efficient iron phosphide catalyst for electrocatalytic hydrogen generation, Bulg. Chem. Commun. 53 (2021) 72–77. https://doi.org/10.34049/bcc.53.1.5323.

[41] T. Chouki, B. Donkova, B. Aktarla, P. Stefanov, S. Emin, Growth of $MoSe_2$ electrocatalyst from metallic molybdenum nanoparticles for efficient hydrogen evolution, Mater. Today Commun. 26 (2021) 101976. https://doi.org/10.1016/j.mtcomm.2020.101976.

[42] M.S. El-Deab, Electrochemical reduction of nitrate to ammonia at modified gold electrodes, Electrochim. Acta. 49 (2004) 1639–1645. https://doi.org/10.1016/j.electacta.2003.11.025.

[43] Y. Luo, L. Tang, U. Khan, Q. Yu, H.M. Cheng, X. Zou, B. Liu, Morphology and surface chemistry engineering toward pH-universal catalysts for hydrogen evolution at high current density, Nat. Commun. 10 (2019) 1–9. https://doi.org/10.1038/s41467-018-07792-9.

[44] Y.P. Zhu, T.Y. Ma, M. Jaroniec, S.Z. Qiao, Self-templating synthesis of hollow Co_3O_4 microtube arrays for highly efficient water electrolysis, Angew. Chemie - Int. Ed. 56 (2017) 1324–1328. https://doi.org/10.1002/anie.201610413.

[45] T. Chouki, M. Machreki, J. Topic, L. Butinar, P. Stefanov, E. Jez, J.S. Summers, M. Valant, A. Fait, S. Emin. Iron phosphide precatalyst for electrocatalytic degradation of rhodamine B dye and removal of Escherichia coli from simulated wastewater, Catalysts. 12 (2022) 269. https://doi.org/10.3390/catal12030269.

[46] E. Szaniawska, I.A. Rutkowska, E. Seta, I. Tallo, E. Lust, P.J. Kulesza, Photoelectrochemical reduction of CO_2: Stabilization and enhancement of activity of copper(I) oxide semiconductor by over-coating with tungsten carbide and carbide-derived carbons, Electrochim. Acta. 341 (2020) 136054. https://doi.org/10.1016/j.electacta.2020.136054.

[47] B.A. López De Mishima, D. Lescano, T. Molina Holgado, H.T. Mishima, Electrochemical oxidation of ammonia in alkaline solutions: Its application to an amperometric sensor, Electrochim. Acta. 43 (1998) 395–404. https://doi.org/10.1016/s0013-4686(97)00061-3.

[48] K.W. Kim, Y.J. Kim, I.T. Kim, G.I. Park, E.H. Lee, Electrochemical conversion characteristics of ammonia to nitrogen, Water Res. 40 (2006) 1431–1441. https://doi.org/10.1016/j.watres.2006.01.042.

[49] N. V. Rees, R.G. Compton, Carbon-free energy: A review of ammonia - and hydrazine-based electrochemical fuel cells, Energy Environ. Sci. 4 (2011) 1255–1260. https://doi.org/10.1039/c0ee00809e.

[50] F. Vitse, M. Cooper, G.G. Botte, On the use of ammonia electrolysis for hydrogen production, J. Power Sources. 142 (2005) 18–26. https://doi.org/10.1016/j.jpowsour.2004.09.043.

[51] I.A. Rutkowska, A. Wadas, P.J. Kulesza, Enhancement of oxidative electrocatalytic properties of platinum nanoparticles by supporting onto mixed WO_3/ZrO_2 matrix, Appl. Surf. Sci. 388 (2016) 616–623. https://doi.org/10.1016/j.apsusc.2016.02.241.

[52] N. Ramaswamy, S. Mukerjee, Influence of inner- and outer-sphere electron transfer mechanisms during electrocatalysis of oxygen reduction in alkaline media, J. Phys. Chem. C. 115 (2011) 18015–18026. https://doi.org/10.1021/jp204680p.

[53] V. Rosca, M.T.M. Koper, Electrocatalytic oxidation of hydrazine on platinum electrodes in alkaline solutions, Electrochim. Acta. 53 (2008) 5199–5205. https://doi.org/10.1016/j.electacta.2008.02.054.

[54] S. Wasmus, E.J. Vasini, M. Krausa, H.T. Mishima, W. Vielstich, DEMS-cyclic voltammetry investigation of the electrochemistry of nitrogen compounds in 0.5 M potassium hydroxide, Electrochim. Acta. 39 (1994) 23–31. https://doi.org/10.1016/0013-4686(94)85006-2.

[55] J. Ibarra, J. Melendres, M. Almada, M.G. Burboa, P. Taboada, J. Juárez, M.A. Valdez, Synthesis and characterization of magnetite/PLGA/chitosan nanoparticles, Mater. Res. Express. 2 (2015) 95010. https://doi.org/10.1088/2053-1591/2/9/095010.

[56] D. Predoi, A. Groza, S.L. Iconaru, G. Predoi, F. Barbuceanu, R. Guegan, M.S. Motelica-Heino, C. Cimpeanu, Properties of basil and lavender essential oils adsorbed on the surface of hydroxyapatite, Materials (Basel). 11 (2018) 1–17. https://doi.org/10.3390/ma11050652.

[57] D. Shao, Q. Wei, Microwave-assisted rapid preparation of nano-ZnO/Ag composite functionalized polyester nonwoven membrane for improving its UV shielding and antibacterial properties, Materials (Basel). 11 (2018) 1412. https://doi.org/10.3390/ma11081412.

[58] P. Bhanja, S. Mishra, K. Manna, K. Das Saha, A. Bhaumik, Porous polymer bearing polyphenolic organic building units as a chemotherapeutic agent for cancer treatment, ACS Omega. 3 (2018) 529–535. https://doi.org/10.1021/acsomega.7b01672.

[59] O.S. Yuzikhin, N.E. Gogoleva, A.I. Shaposhnikov, T.A. Konnova, E. V. Osipova, D.S. Syrova, E.A. Ermakova, V.P. Shevchenko, I.Y. Nagaev, K. V. Shevchenko, N.F. Myasoedov, V.I. Safronova, A.L. Shavarda, A.A. Nizhnikov, A.A. Belimov, Y. V. Gogolev, Rhizosphere bacterium Rhodococcus sp. P1y metabolizes abscisic acid to form dehydrovomifoliol, Biomolecules. 11 (2021) 1–16. https://doi.org/10.3390/biom11030345.

[60] L. Elmlund, P. Söderberg, S. Suriyanarayanan, I.A. Nicholls, A phage display screening derived peptide with affinity for the adeninyl moiety, Biosensors. 4 (2014) 137–149. https://doi.org/10.3390/bios4020137.

[61] N. Sleiman, V. Deluchat, M. Wazne, A. Courtin, Z. Saad, V. Kazpard, M. Baudu, Role of iron oxidation byproducts in the removal of phosphate from aqueous solution, RSC Adv. 6 (2016) 1627–1636. https://doi.org/10.1039/c5ra22444f.

[62] Z. Filip, S. Hermann, K. Demnerová, FT-IR spectroscopic characteristics of differently cultivated Escherichia coli, Czech J. Food Sci. 26 (2008) 458–463. https://doi.org/10.17221/14/2008-cjfs.

[63] Y. Zhu, S. Yang, C. Cao, W. Song, L.J. Wan, Controllable synthesis of carbon encapsulated iron phosphide nanoparticles for the chemoselective hydrogenation of aromatic nitroarenes to anilines, Inorg. Chem. Front. 5 (2018) 1094–1099. https://doi.org/10.1039/c7qi00803a.

[64] N. Norouzi, F.A. Choudhury, H.M. El-Kaderi, Iron phosphide doped, porous carbon as an efficient electrocatalyst for oxygen reduction reaction, ACS Appl. Energy Mater. 3 (2020) 2537–2546. https://doi.org/10.1021/acsaem.9b02250.

[65] R. Liu, J. Chen, Z. Li, Q. Ding, X. An, Y. Pan, Z. Zheng, M. Yang, D. Fu, Preparation of LiFePO$_4$/C cathode materials via a green synthesis route for lithium-ion battery applications, Materials (Basel). 11 (2018) 1–13. https://doi.org/10.3390/ma11112251.

[66] C. Lv, Z. Peng, Y. Zhao, Z. Huang, C. Zhang, The hierarchical nanowires array of iron phosphide integrated on a carbon fiber paper as an effective electrocatalyst for hydrogen generation, J. Mater. Chem. A. 4 (2016) 1454–1460. https://doi.org/10.1039/c5ta08715e.

[67] Y. Zhang, Y. Wang, R. Luo, Y. Yang, Y. Lu, Y. Guo, X. Liu, S. Cao, J.K. Kim, Y. Luo, A 3D porous FeP/rGO modulated separator as a dual-function polysulfide barrier for high-performance lithium sulfur batteries, Nanoscale Horizons. 5 (2020) 530–540. https://doi.org/10.1039/c9nh00532c.

[68] A. Paolella, G. Bertoni, P. Hovington, Z. Feng, R. Flacau, M. Prato, M. Colombo, S. Marras, L. Manna, S. Turner, G. Van Tendeloo, A. Guerfi, G.P. Demopoulos, K. Zaghib, Cation exchange mediated elimination of the Fe-antisites in the hydrothermal synthesis of LiFePO$_4$, Nano Energy. 16 (2015) 256–267. https://doi.org/10.1016/j.nanoen.2015.06.005.

[69] C.M. Chan, L.T. Weng, Surface characterization of polymer blends by XPS and ToF-SIMS, Materials (Basel). 9 (2016) 655. https://doi.org/10.3390/ma9080655.

Highlights:

- Iron phosphide films were synthesized for NO_3^- reduction reaction (NO_3RR) to NH_3.
- *Detection of the in-situ product was achieved using* electrooxidation of NH_3 to N_2.
- Fe_2P film exhibits 96% Faradaic efficiency for NH_3 generation at -0.55 V vs RHE.
- Recycling test showed that FeP electrocatalyst is stable during the NO_3RR.
- DFT (RPBE+D3 level) in an aqueous solution was used to study the NO_3RR mechanism.